The role of intense upper hybrid resonance emissions in the generation of Saturn narrowband emission

J. D. Menietti[1], P. H. Yoon[2,3,4], D. Pisa[5], T. F. Averkamp[1], A. H. Sulaiman[1], W. S. Kurth[1], O. Santolík[5,6], and C. S. Arridge[7]

[1.] Department of Physics and Astronomy, University of Iowa, Iowa City, IA, 52242, USA

[2.] Korea Astronomy and Space Science Institute, Daejeon 34055, Korea

[3.] School of Space Research, Kyung Hee University, Yongin, Gyeonggi 17104, Korea

[4.] Institute for Physical Science and Technology, Univ. of Maryland, College Park, MD 20742, USA

[5.] Department of Space Physics, IAP CAS, Prague, Czechia

[6.] Faculty of Mathematics and Physics, Charles University, Prague, Czechia

[7.] Department of Physics, Lancaster University, Lancaster, UK

Corresponding author: John Douglas Menietti (john-menietti@uiowa.edu)

Key Points:

- Upper hybrid resonances (UHR) occur at Saturn near the magnetic equator on high-inclination inner magnetospheric orbits.
- These regions can be sources of Z-mode and narrowband (NB) emission.
- Observed electron plasma distribution contains a weak loss cone unstable to Z and O mode wave growth.

Abstract

Twenty high-inclination ring-grazing orbits occurred in the final period of the Cassini mission. These orbits intercepted a region of intense Z-mode and narrowband (NB) emission [Ye et al., 2010] along with isolated, intense upper hybrid resonance (UHR) emissions that are often associated with NB source regions. We have singled out such UHR emission seen on earlier Cassini orbits that also lie near the region crossed by the ring-grazing orbits. These previous orbits are important because Cassini electron phase-space distributions are available and dispersion analysis can be performed to better understand the free energy source and instability of the UHR emission. We present an example of UHR emission on a previous orbit that is similar to that observed during the ring-grazing orbits. Analysis of the observed plasma distribution of the previous orbit leads us to conclude that episodes of UHR emission and NB radiation observed during the ring-grazing orbits are likely due to plasma distributions containing loss cones, temperature anisotropies, and strong density gradients near the ring plane. Z-mode emissions associated with UHR and NB emission can be in Landau resonance with electrons to produce scattering or acceleration [Woodfield et al., 2018].

1. Introduction

Gurnett et al. [1981] and Scarf et al., [1982] reported the first observations of narrowband radio emission from Saturn as observed by Voyager. These emissions were in L-O (left-hand ordinary) mode near 5 kHz in the range 3.25 Rs to 58 Rs. (Rs is the radius of Saturn) Ye et al. [2009] have subsequently performed an extensive survey of this emission reporting narrowband (NB) emission near 5 kHz, but also 20 kHz emission and sometimes harmonics of this emission. This emission is believed to originate from the northern and southern edges of the Enceladus density torus. A source mechanism similar to terrestrial continuum emission at Earth was suggested by Ye et al., [2009], where L-O emission is expected when $f_{uh} \sim (n+1/2)f_{ce}$ (f_{ce} = electron cyclotron frequency and n is an integer), where $f_{uh}^2 = f_{ce}^2 + f_{pe}^2$ is the upper hybrid resonance (f_{pe} = electron plasma frequency). Electrostatic cyclotron harmonic (ECH) waves near f_{uh} are frequently observed in space plasmas and are often found to be associated with loss cone electron distributions at the source [Kurth et al., 1979a; Kurth et al., 1979b]. Yoon et al. [1996; 1998a] showed that growth rates of Z-mode are greatly enhanced when $f_{uh}^2 = (nf_{ce})^2$, where n=2 and 3. This Z-mode can escape into free space by a linear mode conversion into ordinary (O) or whistler mode (W) [Horne, 1989].

Menietti et al. [2009] reported observations of NB emission near a source region along the outer edge of the Enceladus source region which displays both L-O and Z-mode emission. The observations included electron phase space distributions near the source region obtained from the low energy electron spectrometer (ELS), part of the Cassini Plasma Spectrometer Investigation (CAPS) [Young et al., 2004]. The proposed generation mechanism was emission occurring when $f_{uh} \sim nf_{ce}$, with significant enhancement of both L-O and particularly Z-mode emission. If strong density gradients are observed within the source region, Z-mode emission can mode convert into O-mode, as suggested by Jones [1976] and Horne [1989] who discussed a similar scenario for the explanation of terrestrial myriametric radiation. Menietti et al. [2009] proposed such a process for the generation of NB emission measured by Cassini.

The Cassini ring-grazing orbits were a series of 20 orbits conducted from November 30, 2016, through April 22, 2017. At this time the spacecraft was at high-inclination with a periapsis of ~ 2.3 R_s. During several of these orbits, near periapsis, the spacecraft observed intense upper hybrid resonances on each side of the equator and these were associated with radio emission in the L-O mode observed at distance from the UHR emission and classified as NB emission. Near the source of the UHR emission, there is stronger emission consistent with Z-mode. However, these observations could not be studied in detail due to the absence of available electron phase space distribution (PSD) data. The low energy electron spectrometer (ELS) that previously provided these data ceased operation earlier in 2009. The morphological similarity of these observations to those observed earlier by Menietti et al. [2009] suggests a similar source mechanism. A re-investigation of Cassini observations at earlier times near regions observed during ring-grazing orbits resulted in the discovery of similar UHR emissions where sufficient ELS data were also available. In this paper we present analysis of electron and UHR emission data for a past Cassini orbit, and compare the results to UHR and radio emission data from a ring-grazing orbit.

Observations

The Cassini Radio and Plasma Wave Science (RPWS) instrument [Gurnett et al., 2004] measures electric (1 Hz to 16 MHz) and magnetic (1 Hz to 12 kHz) oscillations using three nearly orthogonal electric antennas and three orthogonal magnetic search coils. The High Frequency Receiver (HFR, 3.6 kHz-16 MHz) of the Cassini spacecraft provides data for Poynting flux, polarization, and direction-finding capabilities. Details of these data analysis procedures are described in Cecconi and Zarka [2005]. The Cassini Plasma Spectrometer (CAPS) [Young et al., 2004] is composed of three sensors for a study of electrons and ions. We will use data from the electron spectrometer (ELS), which measures electron energies over the range 0.6 eV to 28.25 keV acquired using an 8-detector fan array in a single plane.

In Figure 1 we present a frequency-time spectrogram of wave observations with spectral density color-coded during the ring-grazing orbit near periapsis for day 353 of 2016. At the time Cassini is located at a radial distance $\lesssim 3\ R_s$ and crossed the equator near 21:30 UT where intense broad-banded emission is observed (indicated by the arrow). We note a number of features on this plot that are common during these orbits, which include intense emission above f_{ce} (white line), but near f_{uh} as labeled centered near 21:51 UT and a similar feature centered near 21:08 UT. Narrowband emission (NB) is indicated above f_{ce} at several places. Plasma oscillations (white dots) depict the plasma frequency for $f < f_{ce}$.

Source regions of intense UHR and NB emission have been observed earlier in the Cassini mission during parts of the high-inclination orbits of 2007 and 2008 and at other times. At these times low-energy electron data are often available from the Electron Spectrometer (ELS), however, ELS was not operable during the ring-grazing orbits.

In Figure 2 we show a spectrogram of a perikrone pass for a 4-hour period on day 261 of 2008 that is similar to that shown in Figure 1. Cassini is again crossing the equatorial plane from north to south in the inner magnetosphere with perikrone near 4 R_s at ~17:15 UT. We have indicated several regions of UHR and NB emission. We will focus on the UHR emission near

15:10 UT. Higher resolution data for this time interval are displayed in Figure 3 for a reduced range of frequency and time. The enhancement near 15:10 UT is seen as a narrow-banded emission just above 15 kHz and near f_{uh}. In this plot, f_{uh} is indicated by the (upper, annotated) white line and near the upper extent of the short electrostatic bursts (white dots designate the bursts at several places). We note that the observed UHR emission in the designated source region occurs at a frequency that is somewhat less than $2f_{ce}$. We attribute this to the possibility that Cassini does not intercept the center of the source region, but is observing emission from just above the center or from a nearby field line where f_{ce} is somewhat smaller than the spacecraft measured value. Also indicated in Figure 3 are NB radio emission designated as L-O or fast O-mode and also narrow band R-X or fast X-mode. We present the circular polarization for this emission in Figure 4. The polarization data were obtained from the electric field high frequency receiver (HFR), part of Cassini RPWS investigation (see Cecconi and Zarka [2005] and Ye et al. [2010] for details). The top panel of Figure 4 is the Poynting flux using a relative intensity scale (dB) and the bottom panel displays the circular polarization for a limited time range near the UHR emission source regions. We have indicated both O-mode ("O2" or 2nd harmonic O-mode associated with the UHR source region) and X-mode emission that may be from a more distant source.

The ELS instrument consists of 8 anodes arrayed in a fan each with an approximately 20° x 5° viewing range. During the time of data accumulation the spacecraft was not spinning but the ELS instrument was slowly oscillated by an actuator motor. Figure 5 is a plot of the phase space distribution (PSD) as a function of energy and time for each anode for the time indicated. The pitch angle range of each anode is plotted in the bottom panel. In order to obtain a complete range of pitch angles it is necessary to select the time intervals prudently. During this time a complete energy spectrum is accumulated by all anodes each 4 seconds. To compile a full distribution we have collected data at four time intervals. The anodes were sampling pitch angles in the range 2° to 146° when north of the equatorial plane (Figure 5a). After crossing the magnetic equator a few hours later the spacecraft rotated to allow ELS to monitor pitch angles near 180° (Figure 5b). We have concentrated on the source region near 15:10 in the northern hemisphere with the most intense UHR emission. However, we supplement the observed distribution near 15:10 with data near pitch angles of 180° chosen at a time interval near 18:50 within a similar region of UHR emission and near the same L-shell. In Table 1 we have listed the times of data collection and the pitch angles sampled at each time interval. We note that not all time intervals contain 8 anodes, because some anodes were partially or completely obscured from plasma flux by the spacecraft. We refer readers to Young et al., 2004 and Arridge et al. [2009] for a more complete discussion of the ELS instrument. At 18:53:46 only anodes centered at pitch angles that were not previously sampled were selected. In Figure 6 we enlarge the panels for anode 3 of Figure 5a (nearly field-aligned electrons) and anode 4 of Figure 5b (nearly anti-field-aligned) to more clearly point out the low energy beams and the weak loss cones. Contours of the observed phase space distribution within the source region at 15:10 (with supplemented PSD for pitch angles near 180°) are shown in Figure 7a. This electron distribution is likely to be in a relaxed state considering the 4-second accumulation period for each time interval listed in Table 1.

The electron beam observed in Figure 7a is traveling up the field line away from Saturn in the Northern hemisphere near L ~ 5.2. While extending to energies of a few hundred eV, it is most intense for E < 100 eV. We do not know for certain if any of the beams are unidirectional, but no return beams were observed within the loss cone near 18:55 at L~ 4.8, by which time the Cassini spacecraft had rotated to allow monitoring of electrons from the anti-field-aligned direction. Likewise there is no apparent field-aligned loss cone, perhaps due to its weak nature, having been "filled in" during the rather long integration time (~4 sec). The source of these beams is not known, but similar electron beams at Saturn have been reported in the past. Menietti et al. [2009] investigated intense ECH emission at a similar latitude but L ~ 6.9, in an electron distribution that included a loss cone and an electron beam of E ~ 100 eV, but in that case also, the ELS only monitored the anti-field-aligned hemisphere. These beams can generate beam modes and whistler mode emission via Landau resonance interactions with electrons [cf. Maggs, 1976; Kopf et al., 2010]. Menietti et al. [2009] found that these beams were not responsible for Z-mode emission observed at the same time. Up-going and bi-directional electron beams have been reported at Saturn by Mitchell et al. [2009] in the auroral region for L-shells extending from L < 10 to L > 50. The electron energies were reported to extend from E $\lesssim$ 20 keV (lowest energy level of the low-energy magnetospheric measurement system (LEMMS) on board Cassini) to as high as 1 MeV at times. These authors report that the source region of these electrons appears to be below the satellite. Mitchell et al. [2009] suggest that the auroral region beams have a width that implies a mirror point under 3 Rs, and appear to be accelerated most likely near 1 Rs. The loss cone angle we observe in Figure 7a and the model loss cone in Figure 7b suggest a mirror point < 2 Rs (using the zonal harmonic magnetic field model of Connerney et al. [1982]). The electron beams are of great interest, but they are not a free-energy source of the observed Z-mode or O-mode emission as will be discussed.

Instability and Growth Rate Analysis

To investigate the observed distribution which contains a field-aligned beam and a weak loss cone we will model the observed distribution and investigate the growth of waves using magnetoionic theory as outlined in Yoon et al. [1996; 1998a] where much of the terminology is introduced. In Figure 7b we show a model of the observed electron distribution using a combination of a bi-Maxwellian [Ashour-Abdalla and Thorne, 1978] and a kappa distribution [Yoon, 2014] and a relative color scale. We assume a somewhat more pronounced loss cone with a sharper gradient, because of the probable relaxation of the observed distribution. The model is given in terms of normalized quantity, **u** = **v**/c and μ is the cosine of the electron pitch angle as follows:

$$\begin{aligned}
&\mathscr{F}(u,\mu) = f_0(u,\mu) + f_L(u,\mu) + f_B(u,\mu),\\
&\mathscr{F}_0(u,\mu) = n_0 C_0 \exp\left(-\frac{u^2(1-\mu^2)}{\alpha_{\perp 0}^2} - \frac{u^2\mu^2}{\alpha_{\parallel 0}^2}\right),\\
&\mathscr{F}_L(u,\mu) = n_L C_L \left(1+\frac{u^2}{\kappa\alpha_L^2}\right)^{-\kappa-1}\left(1+\Delta+\tanh\frac{\mu+\mu_0}{\delta}\right),\\
&\mathscr{F}_B(u,\mu) = n_B C_B \exp\left(-\frac{u^2(1-\mu^2)}{\alpha_{\perp B}^2} - \frac{(u\mu-u_0)^2}{\alpha_{\parallel B}^2}\right).
\end{aligned} \tag{1}$$

where $\alpha_\perp$ and $\alpha_\parallel$ are the perpendicular and parallel thermal velocity (normalized to the speed of light, c) and u_0 is the beam parallel drift velocity (normalized to c). Normalization constants are

$$C_0 = \frac{1}{\pi^{3/2}\alpha_{\perp 0}^2 \alpha_{\parallel 0}},$$
$$C_L = \frac{1}{\pi^{3/2}\alpha_L^3}\frac{\Gamma(\kappa+1)}{\kappa^{3/2}\Gamma(\kappa-1/2)}\left[1+\Delta+\frac{\delta}{2}\ln\left(\cosh\frac{1+\mu_0}{\delta}\right)-\frac{\delta}{2}\ln\left(\cosh\frac{1-\mu_0}{\delta}\right)\right]^{-1},$$
$$C_B = \frac{1}{\pi^{3/2}\alpha_{\perp B}^2 \alpha_{\parallel B}} \quad (2)$$

To obtain C_L we made use of the following:

$$\begin{aligned}1 &= 2\pi C_L \int_{-1}^{1} d\mu \left(1+\tanh\frac{\mu+\mu_0}{\delta}\right)\int_0^\infty du u^2 \left(1+\Delta+\frac{u^2}{\kappa\alpha_L^2}\right)^{-\kappa-1} \\ &= \pi^{3/2} C_L \kappa^{3/2}\alpha_L^3 \frac{\Gamma(\kappa-1/2)}{\Gamma(\kappa+1)}\left[1+\Delta+\frac{\delta}{2}\ln\left(\cosh\frac{1+\mu_0}{\delta}\right)-\frac{\delta}{2}\ln\left(\cosh\frac{1-\mu_0}{\delta}\right)\right]\end{aligned} \quad (3)$$

To construct the model shown above we chose the following parameters:

$$\begin{aligned}&\alpha_{\perp 0} = 0.008 = \alpha_{\parallel 0}, \quad n_0 = 1, \\ &\alpha_L = 0.01; \quad \mu_0 = 0.85, \quad \delta = 0.05, \quad \Delta = 0.1, \quad \kappa = 2, \quad n_L = 0.1, \\ &u_0 = 0.025, \quad \alpha_{\perp B} = 0.006, \quad \alpha_{\parallel B} = 0.008, \quad n_B = 0.1.\end{aligned} \quad (4)$$

The magnetoionic (i.e., cold plasma) dispersion relation defined relative to the index of refraction [Melrose, 1986] is specified by

$$N_{X/Z}^2 = 1 - \frac{f_{pe}^2}{f(f+\tau f_{ce})} \qquad N_{W/O}^2 = 1 - \frac{\tau f_{pe}^2}{f(\tau f - f_{ce}\cos^2\theta)} \quad (5)$$

where θ is the wave normal angle (between the wave vector and the ambient magnetic field),

$$\tau = \left(s + \sqrt{s^2 + \cos^2\theta}\right)\frac{f_{pe}^2 - f^2}{\left|f_{pe}^2 - f^2\right|} \qquad s = \frac{ff_{ce}\sin^2\theta}{2\left|f_{pe}^2 - f^2\right|},$$

where the high-frequency cold-plasma (magnetoionic) modes are divided into extraordinary (X) and ordinary (O), but within each mode, separate ranges of frequencies exist. They are as listed below:

- Fast X (or simply X) mode: $\omega > \omega_X$,
- Slow X (or Z) mode: $\omega_Z < \omega < \omega_Z^{res}$,
- Fast O (or simply O) mode: $\omega > \omega_p$,
- Slow O (or W) mode: $0 < \omega < \omega_W^{res}$,

and where cutoff and resonance frequencies introduced are given by

$$\begin{aligned}
\omega_X &= \frac{1}{2}\left(\sqrt{\Omega^2 + 4\omega_p^2} + \Omega\right),\\
\omega_Z &= \frac{1}{2}\left(\sqrt{\Omega^2 + 4\omega_p^2} - \Omega\right),\\
\omega_Z^{res} &= \frac{1}{\sqrt{2}}\left[\omega_{UH}^2 + \sqrt{(\omega_p^2 - \Omega^2)^2 + 4\omega_p^2\Omega^2\sin^2\theta}\right]^{1/2},\\
\omega_W^{res} &= \frac{1}{\sqrt{2}}\left[\omega_{UH}^2 - \sqrt{(\omega_p^2 - \Omega^2)^2 + 4\omega_p^2\Omega^2\sin^2\theta}\right]^{1/2},
\end{aligned} \tag{6}$$

the upper-hybrid frequency ω_{UH} being defined by
$\omega_{UH}^2 = \omega_p^2 + \Omega^2$, where $\omega = 2\pi f$ *and* $\Omega = 2\pi f_{ce}$.

While the dispersion relation is derived from cold plasma theory, the derivation of growth rate assumes an arbitrary (warm) particle distribution function.

Following Yoon et al. [1996; 1998a], the temporal growth rate is then expressed as

$$\gamma_\sigma = \frac{f_{pe}^2}{f}\frac{\pi^2}{R_\sigma}\sum_{s=0}^{\infty}\left(\Theta(sf_{ce}-f)\int_{-1}^{1} d\mu Q_s^\sigma(u_+,\mu) + \Theta(f-sf_{ce})\Theta(1-\mu_s^2)\int_{\mu_s}^{1} d\mu \sum_{+,-} Q_s^\sigma(u_\pm,\mu)\right), \tag{7}$$

$$u_\pm = N_\sigma \mu\cos\theta \pm \sqrt{N_\sigma^2\mu^2\cos^2\theta + 2\left(\frac{sf_{ce}}{f}-1\right)} \text{ (resonant normalized momentum)}, \tag{8}$$

$$\mu_s = \frac{\sqrt{2}}{N_\sigma\cos\theta}\left(1-\frac{sf_{ce}}{f}\right)^{1/2}, \quad b = \frac{f}{f_{ce}}N_\sigma u_\pm\sqrt{1-\mu^2}\sin\theta,$$

Θ (x) is the Heaviside step function, Θ (x) = 1 for x > 0, and Θ (x) = 0 for x ≤ 0, where σ stands for X, Z, W, or O mode and

$$Q_s^{X/Z}(u,\mu) = \frac{\tau^2}{\tau^2+\cos^2\theta}\frac{u^2(1-\mu^2)}{\left|u-N_{X/Z}\mu\cos\theta\right|}\left[\frac{f}{f_{ce}}\left(K_{X/Z}\sin\theta + \frac{\cos\theta}{\tau}(\cos\theta - N_{X/Z}u\mu)\right)\right.$$
$$\left.\times\frac{J_s(b)}{b} + J'_s(b)\right]^2\left(u\frac{\partial}{\partial u} + (N_{X/Z}u\cos\theta-\mu)\frac{\partial}{\partial\mu}\right)f(u,\mu), \tag{9}$$

$$Q_s^{O/W}(u,\mu)=\frac{1}{\tau^2+\cos^2\theta}\frac{u^2(1-\mu^2)}{\left|u-N_{O/W}\mu\cos\theta\right|}\left[\frac{f}{f_{ce}}\left(K_{O/W}\sin\theta\cos\theta-\tau(\cos\theta-N_{O/W}u\mu)\right)\right.$$
$$\left.\times\frac{J_s(b)}{b}+\cos\theta J'_s(b)\right]^2\left(u\frac{\partial}{\partial u}+(N_{O/W}u\cos\theta-\mu)\frac{\partial}{\partial\mu}\right)f(u,\mu),$$

with subscript s = X, W, or O and where

$J_s(b)$ is the Bessel function of the first kind of order s

$J'_s(b)=\dfrac{\partial J_s(b)}{\partial b}$

$$\mathrm{K}_{X/Z}=\frac{\omega_p^2}{\omega_p^2-\omega^2}\frac{\Omega\sin\theta}{\omega+\tau\Omega},\quad \mathrm{K}_{O/W}=\frac{\omega_p^2}{\omega_p^2-\omega^2}\frac{\tau\Omega\sin\theta}{\tau\omega-\Omega\cos^2\theta},$$
$$T_{X/Z}=\frac{\cos\theta}{\tau},\quad T_{O/W}=\frac{\tau}{\cos\theta},$$
$$R_{X/Z}=1+\frac{\omega_p^2\left(\tau^2\omega^2-\omega_p^2\cos^2\theta\right)}{\omega^2\left(\omega+\tau\Omega\right)^2\sin^2\theta}\frac{\tau^2-\cos^2\theta}{\tau^2+\cos^2\theta},$$
$$R_{O/W}=1+\frac{\omega_p^2\cot^2\theta\left(\tau^2\omega_p^2-\omega^2\cos^2\theta\right)}{\omega^2\left(\tau\omega-\Omega\cos^2\theta\right)^2}\frac{\tau^2-\cos^2\theta}{\tau^2+\cos^2\theta},$$

The terms K and R are parameters that arise from the theory of the magnetoionic dispersion relation [cf. Yoon et al., 1996]. K is related to the unit electric field vector associated with the wave, and R is related to the radial group velocity.

To complete the temporal growth rate one needs to consider the quantity,

$$
\begin{aligned}
& u\frac{\partial \mathcal{F}}{\partial u}+\left(N_\sigma u\cos\theta-\mu\right)\frac{\partial \mathcal{F}}{\partial \mu} \\
& =-\frac{2n_0u^2}{\pi^{3/2}\alpha_{\perp 0}^4\alpha_{\parallel 0}}\left[1+N_\sigma u\mu\cos\theta\left(\frac{\alpha_{\perp 0}^2}{\alpha_{\parallel 0}^2}-1\right)\right]\exp\left[-\frac{u^2}{\alpha_{\perp 0}^2}-\frac{u^2\mu^2}{\alpha_{\perp 0}^2}\left(\frac{\alpha_{\perp 0}^2}{\alpha_{\parallel 0}^2}-1\right)\right] \\
& -\frac{2n_Bu^2}{\pi^{3/2}\alpha_{\perp B}^4\alpha_{\parallel B}}\left[1+N_\sigma u\mu\cos\theta\left(\frac{\alpha_{\perp 0}^2}{\alpha_{\parallel 0}^2}-1\right)+N_\sigma u_0\cos\theta\frac{\alpha_{\perp B}^2}{\alpha_{\parallel B}^2}\right]\exp\left(-\frac{u^2\left(1-\mu^2\right)}{\alpha_{\perp B}^2}-\frac{(u\mu+u_0)^2}{\alpha_{\parallel B}^2}\right)
\end{aligned}
\tag{11}
$$

$$
\begin{aligned}
& -\frac{n_L}{\pi^{3/2}\alpha_L^3}\frac{1}{1+\Delta+\dfrac{\delta}{2}\ln\dfrac{\cosh(1+\mu_0)}{\cosh(1-\mu_0)}}\frac{\Gamma(\kappa+1)}{\kappa^{3/2}\Gamma(\kappa-1/2)}\left(1+\frac{u^2}{\kappa\alpha_L^2}\right)^{-\kappa-2} \\
& \qquad \left[\frac{2u^2}{\alpha_L^2}\frac{\kappa+1}{\kappa}\left(1+\Delta-\tanh\frac{\mu-\mu_0}{\delta}\right)+\frac{1}{\delta}\left(N_\sigma u\cos\theta-\mu\right)\left(1+\frac{u^2}{\kappa\alpha_L^2}\right)\left(1-\tanh^2\frac{\mu-\mu_0}{\delta}\right)\right]
\end{aligned}
$$

In Figures 8a,b we plot the growth rate, γ_{max}/Ω versus ω_p/Ω for the model distribution of Figure 7b. The maximum growth rates are determined by surveying both ω/Ω and θ. We plot the maximum growth rate for the Z-mode (8a) and O mode (8b) ("2" refers to 2nd harmonic emission, $f/f_{ce} \sim 2$). The fundamental emission (Z1 and O1) refer to emission observed in Figure 1 near 21:50. For day 261 of 2008, the UHR emission at ~15:10 is near the 2nd harmonic. In Figure 8a Z2 mode begins to grow for $\omega_p/\Omega > \sqrt{3}$, with $\gamma_{max} \sim 4.5\text{x}10^{-1}\,\Omega$, assuming a ratio of the warm $(n_L + n_B)$ to total density, $n_w/n_o= 10^{-2}$ (right ordinate scale). This ratio is consistent with the observed distribution of Figure 7a. For the Cassini perikrone pass of Figure 1 (ring-grazing orbit), the value of ω_p/Ω is lower as seen near the UHR emission centered close to 21:50:36 in Figure 1, with $f_{uh}/f_{ce} \sim 1.25$ and $\omega_p/\Omega \sim 0.74$. For this source region we do not have PSD observations. However, using the same model electron phase space distribution function of

Figure 7b, but reducing $n_w/n_o=10^{-4}$ (left scale) we find Z1 growth rates $\gamma_{max} \sim 1.5x10^{-2}\,\Omega$ for $\omega_p/\Omega \sim 0.74$ (near 21:50:36 of Figure 1), falling to 0 for $\omega_p/\Omega = \sqrt{2}$.

The growth rates shown in Figure 8b are similarly shown with $n_w/n_o = 10^{-2}$ (right scale) and $n_w/n_o = 10^{-4}$ (left scale). O-mode growth rates are much weaker than those for Z-mode. X-mode is also unstable but with growth rates weaker than Z-mode. We observe X3 emission (Figure 4), but not X2. We hypothesize that the source region of the observed X-mode bands may be more distant Cassini spacecraft. The Z-mode growth rate as a function of frequency and wave normal angle is shown in Figure 9 for frequencies near the 2nd harmonic (Z2) and a value of ω_p/Ω close to that near the source region (Figure 3). One can see that the Z-mode growth rate peaks at large wave normal angles.

We can estimate the gain and growth length (e-folding distance) of the Z2 emission. The bursts of upper hybrid resonance emission occur with spectra density $I_o \sim 10^{-14}\ V^2/(m^2Hz)$, and maybe the seed for the growth of the Z-mode. The Z-mode maximum spectral density is $\sim 10^{-11}\ V^2/(m^2Hz)$. We, therefore, estimate the gain to be $G_z = I/I_o = 10^3 = \exp(2\ \gamma\ L_z / v_g)$, where L_z is the growth distance and v_g is the group velocity of the Z-mode. In Figure 10a we plot the group velocity versus ω_p/Ω for both the Z1 and Z2 emission. For $\omega_p/\Omega \sim 1.8$ $v_g \sim 10^7$ m/s, so we estimate $L = v_g \ln(G) / (2\ \gamma) \sim 2.2$ km for the scale size of the source region. From the electron beam temperature we estimate the gyroradius of the beam plasma to be < 100 m.

In order to estimate the gain for the O-mode we note from Figure 8b that the maximum growth rate for O2 is $\gamma_{max} < 10^{-6}\,\Omega$ for $\omega_p/\Omega \sim 1.8$. The weakest observable O-mode emission observed on Figure 3 has a spectral density of $I_o \sim 10^{-15}$ $V^2/(m^2Hz)$, while the maximum spectral density is $I \sim 10^{-13}$ $V^2/(m^2Hz)$. We therefore estimate the gain to be $G_o = I/I_o \sim 10^2$. From Figure 10b, we obtain for O2 emission, $v_{gr} \sim 0.48c$. In the same manner as for the Z-mode, we estimate L_{o2} = 5.6 x 10^6 km. We estimate the size of the source region by noting the region of large Z-mode intensity extending from perhaps 14:40 to 15:15 in Figure 3. At this time the spacecraft velocity is ~15.5 km/sec, so the approximate source size $L_s \sim 3.3x10^4$ km. This value is about 2 orders of magnitude less than L_{o2} = 5.6 x 10^6 km. Using a similar estimate of the approximate size of the O1 source region near 21:50 UT of Figure 1 yields another large value of L_{o1} =5.7 x 10^7 km for the growth length. For the O1 emission of Figure 1 we estimate the source size to be 1.67x10^4 km, which is over 3 orders of magnitude less than L_{o1}=5.7x10^7 km. These large estimates imply that there may be another source for the observed O-mode emission.

O1 growth rates are lower than Z1, but are modest with $\gamma_{max} \sim 1.9x10^{-5}\ \Omega$ for $\omega_p/\Omega \sim 0.74$. The lowest observable O-mode in Figure 1 is $I_o \sim 2x10^{-16}$ $V^2/(m^2Hz)$, while the maximum value is ~ 4x10^{-15} $V^2/(m^2Hz)$, so we estimate the O1 gain to be ~ 2 x 10^2. From Figure 10b we obtain v_g = 0.67c, and we obtain an estimated growth length of L ~ 5.7 x 10^7 km, which is also quite large, implying another source for the O-mode. We can increase the O-mode growth rate significantly by increasing the depth and steepness of the phase space density gradient of the model loss cone, but this requires additional assumptions. However, we may also consider Z-mode to O-mode conversion near a density gradient as previous authors have discussed.

Near the Z-mode source region we calculate the cold plasma index of refraction based on the measured values of f_{pe} = 16.65 kHz, f_{ce} = 9.5 kHz for Z-mode wave normal angles θ = 0-4° and for θ = 0° for O-mode. We assume a small wave normal angle for the Z-mode after refraction at the density gradient near the edge of the Enceladus plasma torus. In Figure 11 we plot these indices as a function of frequency, with the indices agreeing for θ = 0 at f_{pe}. The rapid change of magnitude of f_{uh} near the Z-mode source region in Figure 3 indicates a strong density gradient during this time. This suggests that mode conversion from Z-mode to O-mode can occur through the "radio window" [Jones, 1976; 1980; Horne, 1989; Yoon et al., 1998b] as the Z-mode is refracted to small wave normal angles as it propagates. This could appreciably enhance the observed O-mode intensity [cf. Horne, 1989].

Summary and Conclusions

Observations of intense UHR emission and associated NB emission in the O and Z-modes were obtained during some Cassini ring-grazing orbits in the final phase of mission. These orbits had a high inclination with a periapsis near 2.3 R_S, similar to some earlier Cassini orbits during periods from late 2007 to early 2009. This fact has been important in our investigation of the source mechanism for these emissions, because ELS data were not available during the ring-grazing orbits. Critical to the calculation of growth rate is a complete electron phase space distribution. Within the source region, the pitch angle coverage ranged from 2° < α < 146° while the Cassini spacecraft was north of the equator. However, electron observations of the ELS for α > 150° were available for southern latitudes during this orbit. Within a similar source region near the same L-shell in the southern hemisphere, observations revealed a weak loss cone which is the free energy source for these emissions.

Because the accumulation time for the ELS phase space distributions is ~4 seconds, we have modeled the PSD by modestly enhancing the observed loss cone, assuming that some filling of the loss cone occurred during the sampling accumulation time. With these assumptions, we can obtain Z-mode emission with sufficient growth and gain to explain the observations. O-mode growth rates appear to be too low to explain the observed O-mode intensity. Increasing the depth and phase space density gradient of the model loss cone would increase the O-mode intensity. However, there is an opportunity for mode conversion of Z-mode to O-mode to explain the observations of O-mode intensity. Finally, weak X-mode is observed, but this emission appears to be from a remote source, with no local strong enhancement of upper hybrid resonance observed at the X-mode frequency.

The observations of intense UHR and NB emission during the ring-grazing orbit of Figure 1 are similar to those of Figures 2 and 3 for which we have electron PSD data and the growth rate calculations are performed. However, for the observations of Figure 1 the ratio of f_{pe}/f_{ce} is lower, with $f_{uh} \sim f_{ce}$ near the intense UHR source region. We have repeated the growth calculations for the model PSD of Figure 4 with $f_{uh}/f_{ce} \sim 1$ and with a reduced ratio of $n_w/n_o = 10^{-4}$. The growth rates, shown in Figure 8, indicate the feasibility of the proposed instability to explain the intense UHR emission for the observations during the Cassini ring-grazing orbit shown in Figure 1. O-mode growth was found to be insufficient for the case of O1 and O2 emission. However, it is conceivable that mode conversion from Z-mode to O-mode can occur near the observed strong density gradient. The results indicate that intense UHR emissions and associated NB radio emissions can be a result of plasma distributions containing loss cones and temperature anisotropies near regions of strong density gradients close to the Saturn ring plane of the inner magnetosphere.

Determining the source generation mechanism of the nearly ubiquitous NB and UHR emission is scientifically important. Z-mode emission may be a significant source of electron scattering and acceleration at Saturn [Woodfield et al., 2018], and these waves are observed much more prominently at Saturn than at Earth [Menietti et al., 2016]. A better knowledge of the generation mechanism of this emission is important to understand local and global mechanisms of Saturn magnetospheric plasma energy distribution.

Acknowledgments

We wish to thank J. Barnholdt and K. Kurth for administrative assistance and J. Chrisinger for assistance with the figures. JDM acknowledges support from JPL contract 14150 and NASA grant NNX16AI47G. P.H.Y. acknowledges the Science Award Grant from the GFT Charity, Inc., to the University of Maryland, and the BK21 plus program from the National Research Foundation (NRF), Korea, to Kyung Hee University. DP and OS were supported by grant 17-08772S of Czech Science Foundation (GACR). OS acknowledges support from the Czech Academy of Sciences through the Praemium Academiae Award. Cassini RPWS data are archived in calibrated full resolution at the NASA Planetary Data System website: http://pds.nasa.gov/.

REFERENCES

Arridge, C. S., Gilbert, L. K., Lewis, G. R., Sittler, E. C., Jones, G. H., Kataria, D. O., et al. (2009), The effect of spacecraft radiation sources on electron moments from the Cassini CAPS electron spectrometer, *Planetary and Space Science,* 57(7), 854-868. https://doi.org/10.1016/j.pss.2009.02.011

Ashour-Abdalla, M., & Thorne, R. M. (1978), Toward a unified view of diffuse auroral precipitation, *Journal of Geophysical Research*, 83(A10), 4755-4766. https://doi.org/10.1029/JA083iA10p04755

Cecconi, B., & Zarka, P. (2005), Direction finding and antenna calibration through analytical inversion of radio measurements performed using a system of two or three electric dipole antennas on a three-axis stabilized spacecraft, *Radio Science,* 40, RS3003. https://doi.org/10.1029/2004RS003070

Connerney, J. E. P., Ness, N. F., & Acuna, M. H. (1982), Zonal harmonic model of Saturn's magnetic field from Voyager 1 and 2 observations, *Nature,* 298, 44-66. https://doi.org/10.1038/298044a0

Gurnett, D. A., Kurth, W. S., & Scarf, F. L. (1981), Narrowband electromagnetic emissions from Saturn's magnetosphere, *Nature,* 292, 733-737. https://doi.org/10.1038/292733a0

Gurnett, D. A., Kurth, W. S., Kirchner, D. L., Hospodarsky, G. B., Averkamp, T. F., Zarka, P., et al. (2004), The Cassini radio and plasma wave investigation, *Space Science Reviews*, 114, 395-463. https://doi.org/10.1007/s11214-004-1434-0

Horne, R. B. (1989), Path-integrated growth of electrostatic waves: The generation of terrestrial myriametric radiation, *Journal of Geophysical Research,* 94(A7), 8895-8909. https://doi.org/10.1029/JA094iA07p08895

Jones, D. (1976), Source of terrestrial non-thermal continuum radiation, *Nature, 260*, 686-689. https://doi.org/10.1038/260686a0

Jones, D. (1980), Latitudinal beaming of planetary radio emissions, *Nature, 288,* 225-229. https://doi.org/10.1038/288225a0

Kopf, A. J., Gurnett, D. A., J. D. Menietti, Schippers, P., Arridge, C. S., Hospodarsky, G. B., Kurth, W. S., Grimald, S., Andre, N., Coates, A. J., & Dougherty, M. K. (2010), Electron beams as the source of whistler-mode auroral hiss at Saturn, *Geophysical Research Letters,* 37, L09102. https://doi.org/10.1029/2010GL042980

Kurth, W. S., Ashour-Abdalla, M, Frank, L. A., Fennel, C. F., Gurnett, D. A., Sentman, D. D., & Burek, B. G. (1979a), A comparison of intense electrostatic waves near f_{UHR} with linear instability theory, *Geophysical Research Letters,* 6(6), 487-490. https://doi.org/10.1029/GL006i006p00487

Kurth, W. S., Craven, J. D., Frank, L. A., & Gurnett, D. A. (1979b), Intense electrostatic waves near the upper hybrid resonance frequency, *Journal of Geophysical Research,* 84(A8), 4145-4164. https://doi.org/10.1029/JA084iA08p04145

Maggs, J. E., (1976), Coherent generation of VLF hiss, *Journal of Geophysical Research,* 81(10), 1707-1724. https://doi.org/10.1029/JA081i010p01707

Melrose, D. B. (1986), Instabilities in Space and Laboratory Plasmas, pp. 170-172, Cambridge University Press, Cambridge.

Menietti, J. D., Averkamp, T. F., Ye, S.-Y., Horne, R. B., Woodfield, E. E., Shprits, Y. Y., Gurnett, D. A., Persoon, A. M., & Wahlund, J.-E. (2015), Survey of Saturn Z-mode emission, *Journal of Geophysical Research,* 120, 6176-6187. https://doi.org/10.1002/2015JA021426

Menietti, J. D., Ye, S.-Y., Yoon, P. H., Santolík, O., Rymer, A. M., Gurnett, D. A., & Coates, A. J. (2009), Analysis of narrowband emission observed in the Saturn magnetosphere, *Journal of Geophysical Research,* 114(A6). https://doi.org/10.1029/2008JA013982

Mitchell, D. G., Kurth, W. S., Hospodarsky, G. B., Krupp, N., Saur, J., Mauk, B. H., Carbary, J. F., Krimigis, S. M., Dougherty, M. K., & Hamilton, C. C. (2009), Ion conics and electron beams associated with auroral process on Saturn, *Journal of Geophysical Research,* 114, A02212. https://doi.org/10.1029/2008JA013621

Scarf, F. L., Gurnett, D. A., Kurth, W. S., & Poynter, R. L. (1982), Voyager 2 plasma-wave observations at Saturn, *Science,* 215(4532), 587-594. https://doi.org/10.1126/science.215.4532.587

Woodfield, E. E., Horne, R. B., Glauert, S. A., Menietti, J. D., Shprits, Y. Y., & Kurth, W. S. (2018), Formation of electron radiations belts at Saturn by Z-mode wave acceleration, *Nature Communications,* Vol. 9, Article 5062. https://doi.org/10.1038/s41467-018-07549-4

Ye, S.-Y., Gurnett, D. A., Fischer, G., Cecconi, B., Menietti, J. D., Kurth, W. S., et al. (2009), Source locations of narrowband radio emissions detected at Saturn, *Journal of Geophysical Research,* 114(A6), A06219. https://doi.org/10.1029/2008JA013855

Ye, S.-Y., Menietti, J. D., Fischer, G., Wang, Z., Cecconi, B., Gurnett, D. A., & Kurth, W. S. (2010), Z mode waves as the source of Saturn narrowband radio emissions, *Journal of Geophysical Research,* 115, A08228. https://doi.org/10.1029/2009JA015167

Yoon, P. H., Weatherwax, A. T., Rosenberg, T. J., & LaBelle, J. (1996), Lower ionospheric cyclotron maser theory: A possible source of $2f_{ce}$ and $3f_{ce}$ auroral radio emissions, *Journal of Geophysical Research,* 101(A12), 27,015-27,025. https://doi.org/10.1029/96JA02664

Yoon, P. H., Weatherwax, A. T., & Rosenberg (1998a), On the generation of auroral radio emissions at harmonics of lower ionospheric electron cyclotron frequency: X, O, and Z mode maser calculations, *Journal of Geophysical Research,* 103(A3), 4071-4078. https://doi.org/10.1029/97JA03526

Yoon, P. H., Weatherwax, A. T., Rosenberg, T. J., LaBelle, J., & Shepherd, S. G. (1998b), Propagation of medium frequency (1–4 MHz) auroral radio waves to the ground via the Z-mode radio window*, Journal of Geophysical Research,* 103(A12), 29,267-29,275. doi:10.1029/1998JA900032

Yoon, P. H. (2014) Electron kappa distribution and quasi-thermal noise, *Journal of Geophysical Research,* 119(9), 7074-7087. https://doi.org/10.1002/2014JA020353

Young, D. T., Berthelier, J. J., Blanc, M., Burch, J. L., Coates, A. J., Goldstein, R., et al. (2004), Cassini Plasma Spectrometer Investigation, *Space Science Reviews,* 114, 1-112. https://doi.org/10.1007/s11214-004-1406-4

Table 1 Non-obstructed Anodes							
Time	**Central Pitch Angle (degs)**						
15:07:34	113	131	146				
15:08:14	83	96	108	119	127		
15:11:30	2	18	21	38	41	61	81
18:53:46	158	161	176				

Figure Captions

Figure 1

A frequency-time spectrogram of wave observations with power spectral density color-coded during the ring-grazing orbit near periapsis for day 353 of 2016. Cassini is located at the radial distance ~ 3 R_S during the equator crossing near 21:30 UT (shown by the black arrow), where intense broad-banded emission is observed. Intense UHR emission is indicated as f^*_{uh}.

Figure 2

A spectrogram of a perikrone pass for a 4-hour period on day 261 of 2008 is similar to the pass shown in Figure 1. Cassini is again crossing the equatorial plane near 17:15 UT from north to south in the inner magnetosphere with perikrone at the radial distance ~4 R_S.

Figure 3

A detailed frequency-time spectrogram with a higher resolution for a reduced range of frequencies and time from Figure 2. The enhancement near 15:10 UT is seen as a narrow-banded emission just above 15 kHz and near f_{uh}. White dots indicate f_{uh} at the upper extent of some of the short electrostatic bursts.

Figure 4

The top panel is the Poynting flux using a relative (to background) intensity scale (dB) and the bottom panel displays the circular polarization for a limited time range near the intense UHR emission source region. Circular polarization in the O, X, and Z-modes are labeled.

Figure 5

The phase space distribution (PSD) as a function of energy and time for each of the 8 anodes for the time indicated. The pitch angle range of each anode is plotted in the bottom panel. During the time of data accumulation the ELS instrument was slowly oscillated by an actuator motor. White arrows in the left panel indicate low energy field-aligned electron beams. White arrows in the right panel indicate loss cones.

Figure 6

Enlargement of the panels for anode 3 of (5a) (nearly field-aligned electrons) and anode 4 of (5b) (nearly anti-field-aligned electrons). The low energy beams and the weak loss cones are more apparent. Arrows indicate the (a) electron beams, and (b) the loss cones.

Figure 7

A model of the observed distribution using a combination of a bi-Maxwellian and a kappa distribution. The color bar is a relative scale.

Figure 8

The maximum growth rate, γ/Ω versus ω_p/Ω for the model distribution. We plot the maximum growth rate for the Z-mode (a) and both O and X modes (b) ("2" refers to 2^{nd} harmonic emission, $f/f_{ce} \sim 2$). In (a,b) the left ordinate axis is for Z1 and O1 ($n_w/n_0 = 10^{-4}$) and the right ordinate axis is for Z2 and O2 ($n_w/n_0 = 10^{-2}$).

Figure 9

The Z-mode growth rate as a function of frequency and wave normal angle for frequencies near the 2^{nd} harmonic (Z2) and a value of $\omega_p/\Omega = 1.75$, close to that near the source region.

Figure 10

The group velocity versus ω_p/Ω for both the Z1 and Z2 emission. For For $\omega_p/\Omega \sim 1.8$, $v_g \sim 10^7$ m/s.

Figure 11

Cold plasma index of refraction versus frequency and wave normal angle (Θ) for the Z-mode and O-mode for f_{pe} = 16.65 kHz, f_{ce}= 9.5 kHz near the Z-mode source region. The O-mode is evaluated at Θ = 0°, while the Z-mode is evaluated for Θ = 0, 1°, 2°, 3°, and 4° The indices agree for Θ = 0° at f_{pe} where mode conversion from Z-mode to O-mode can occur through the "radio window" as the Z-mode is refracted to small wave normal angles within the density gradient.

Figure 1.

A-D18-067-4

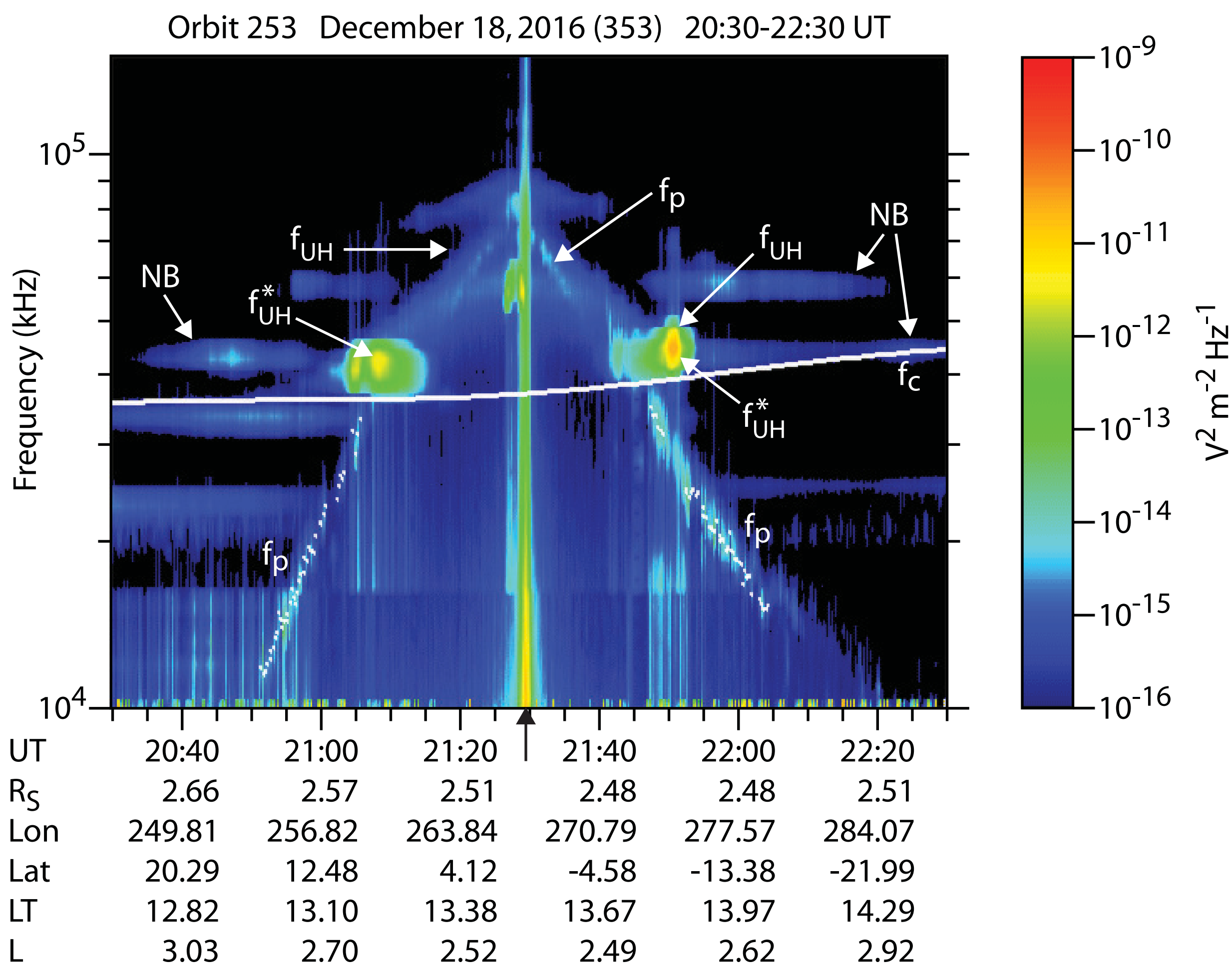

Orbit 253 December 18, 2016 (353) 20:30-22:30 UT
Frequency (kHz)
10^5
10^4
NB
f_{UH}^*
f_{UH}
f_p
f_{UH}
NB
f_c
f_{UH}^*
f_p
f_p
10^{-9}
10^{-10}
10^{-11}
10^{-12}
10^{-13}
10^{-14}
10^{-15}
10^{-16}
$V^2\ m^{-2}\ Hz^{-1}$
UT 20:40 21:00 21:20 21:40 22:00 22:20
R_S 2.66 2.57 2.51 2.48 2.48 2.51
Lon 249.81 256.82 263.84 270.79 277.57 284.07
Lat 20.29 12.48 4.12 -4.58 -13.38 -21.99
LT 12.82 13.10 13.38 13.67 13.97 14.29
L 3.03 2.70 2.52 2.49 2.62 2.92

Figure 2.

A-D19-020

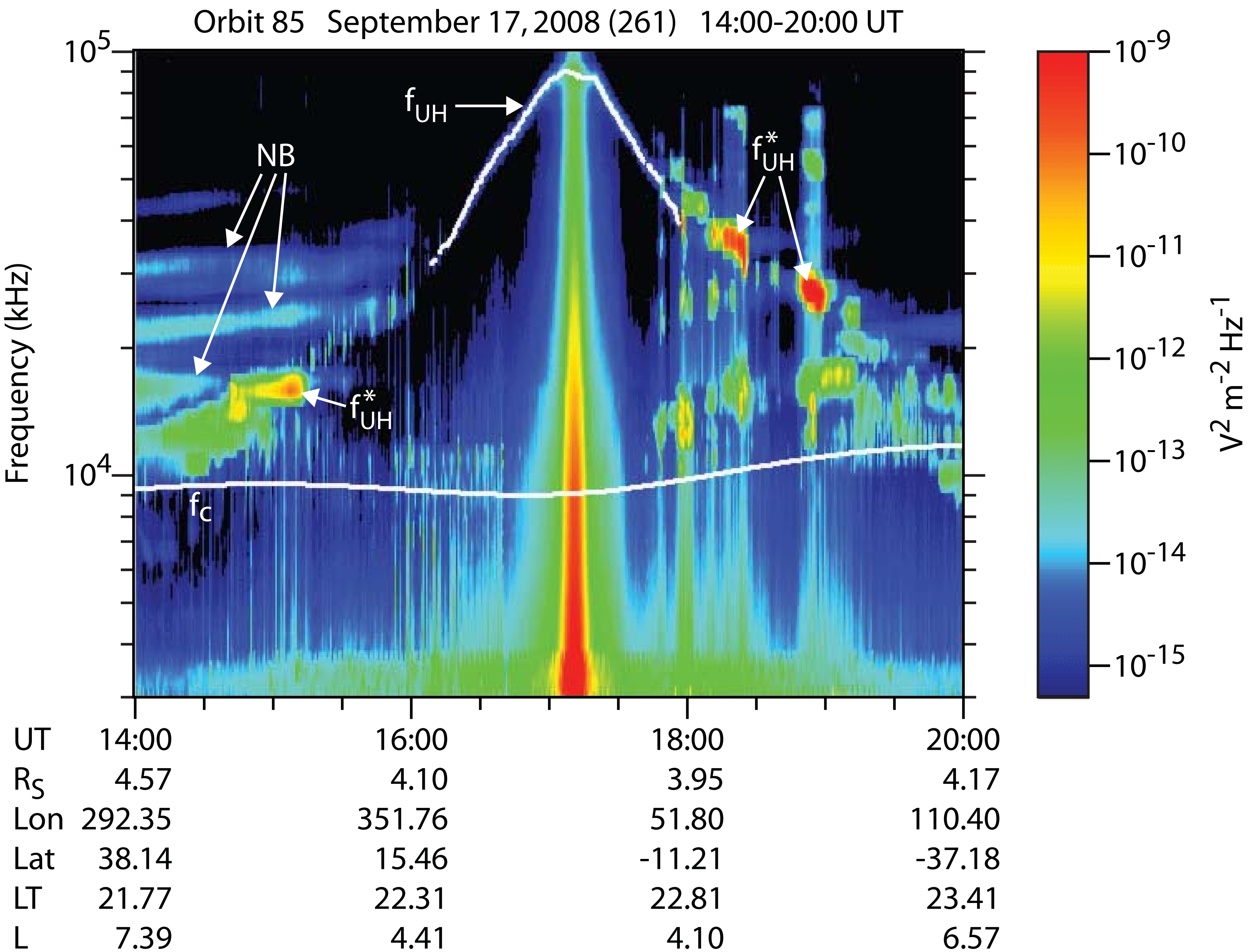

Orbit 85 September 17, 2008 (261) 14:00-20:00 UT
Frequency (kHz)
10^5
10^4
f_{UH}
NB
f_{UH}^*
f_{UH}^*
f_c
$V^2\ m^{-2}\ Hz^{-1}$
10^-9
10^-10
10^-11
10^-12
10^-13
10^-14
10^-15
UT 14:00 16:00 18:00 20:00
R_S 4.57 4.10 3.95 4.17
Lon 292.35 351.76 51.80 110.40
Lat 38.14 15.46 -11.21 -37.18
LT 21.77 22.31 22.81 23.41
L 7.39 4.41 4.10 6.57

Figure 3.

A-D19-021-1

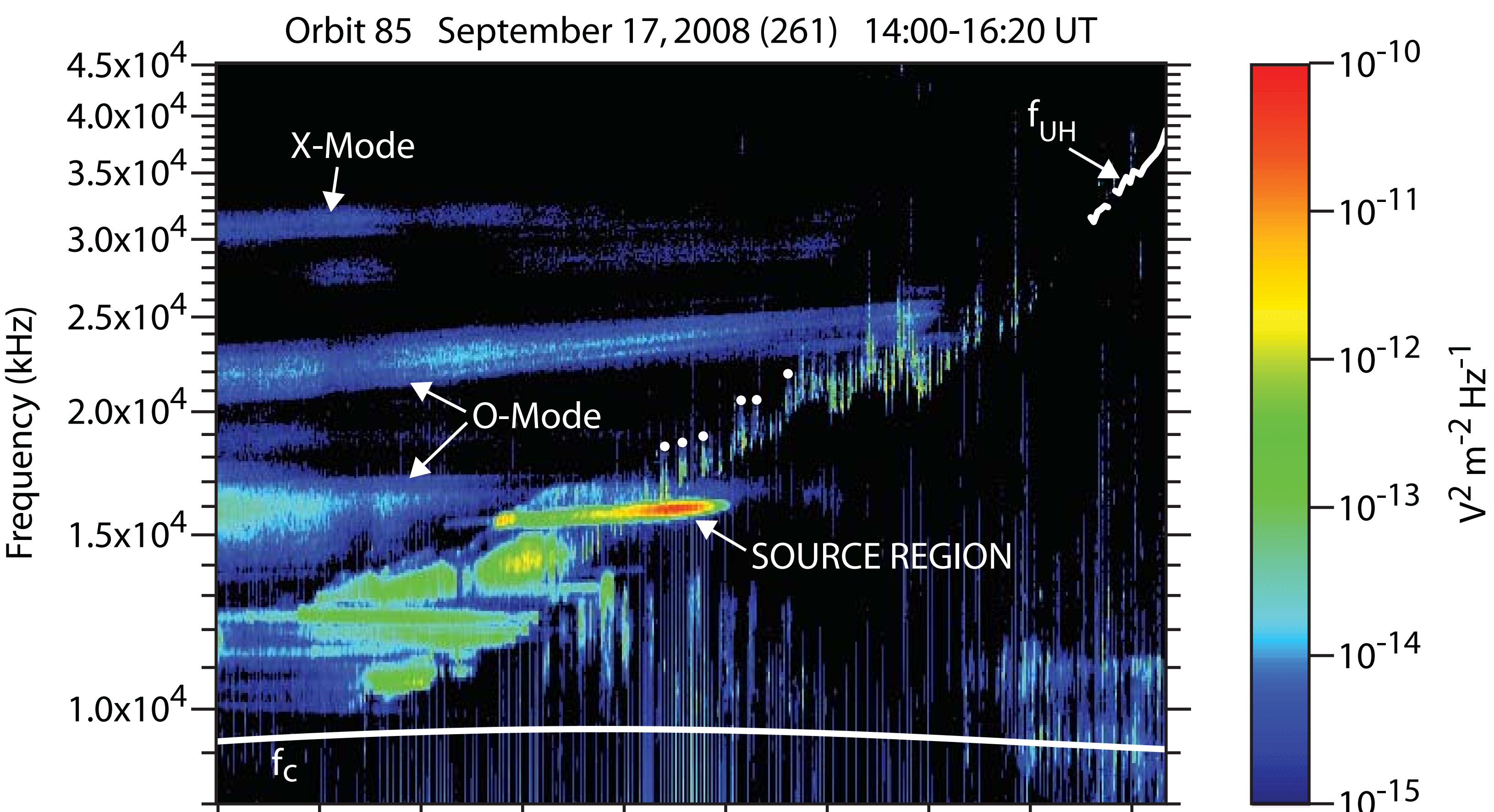

UT	14:00	15:00	16:00
R_S	4.57	4.30	4.10
Lon	292.35	321.86	351.76
Lat	38.14	27.48	15.46
LT	21.77	22.05	22.31
L	7.39	5.47	4.41

Figure 4.

A-D19-023-2

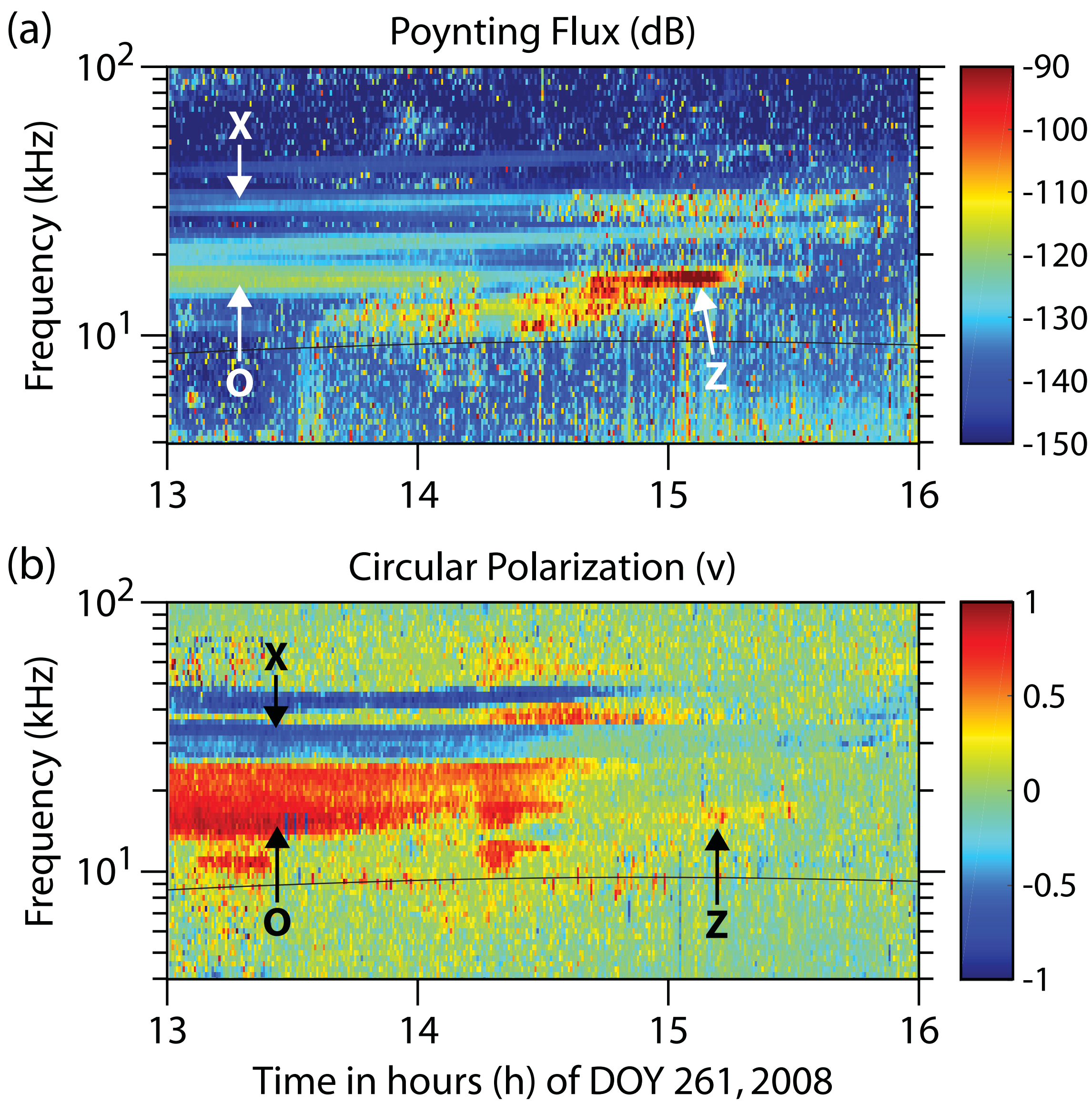
(a)
Poynting Flux (dB)
Frequency (kHz)
X
O
Z
-90
-100
-110
-120
-130
-140
-150
13
14
15
16
(b)
Circular Polarization (v)
Frequency (kHz)
X
O
Z
1
0.5
0
-0.5
-1
13
14
15
16
Time in hours (h) of DOY 261, 2008

Figure 5.

A-D19-032

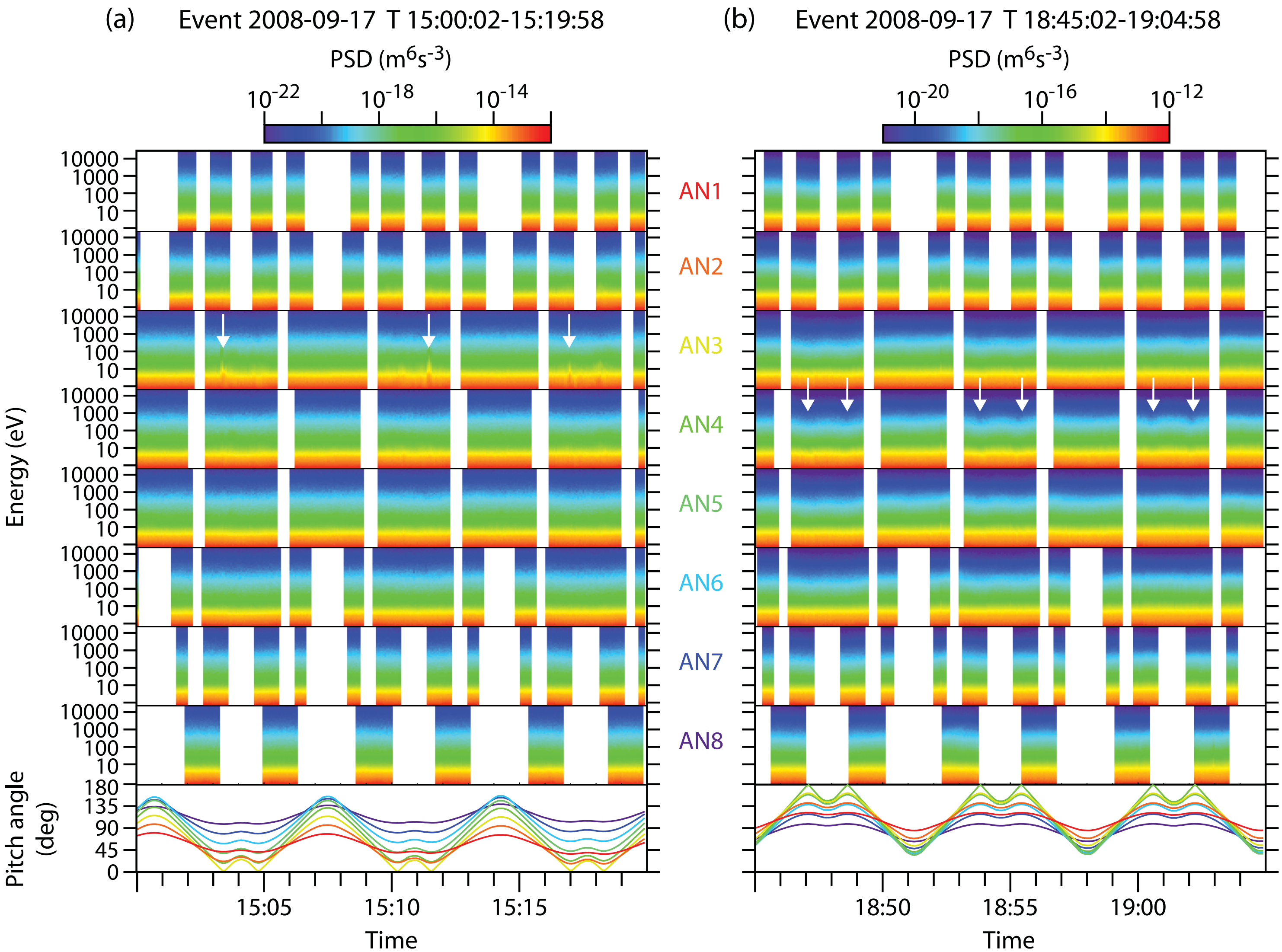
(a) Event 2008-09-17 T 15:00:02-15:19:58
PSD (m^6s^{-3})
10^{-22} 10^{-18} 10^{-14}
(b) Event 2008-09-17 T 18:45:02-19:04:58
PSD (m^6s^{-3})
10^{-20} 10^{-16} 10^{-12}
AN1
AN2
AN3
AN4
AN5
AN6
AN7
AN8
Energy (eV)
10000
1000
100
10
Pitch angle (deg)
180
135
90
45
0
15:05
15:10
15:15
18:50
18:55
19:00
Time

Figure 6.

A-D19-040

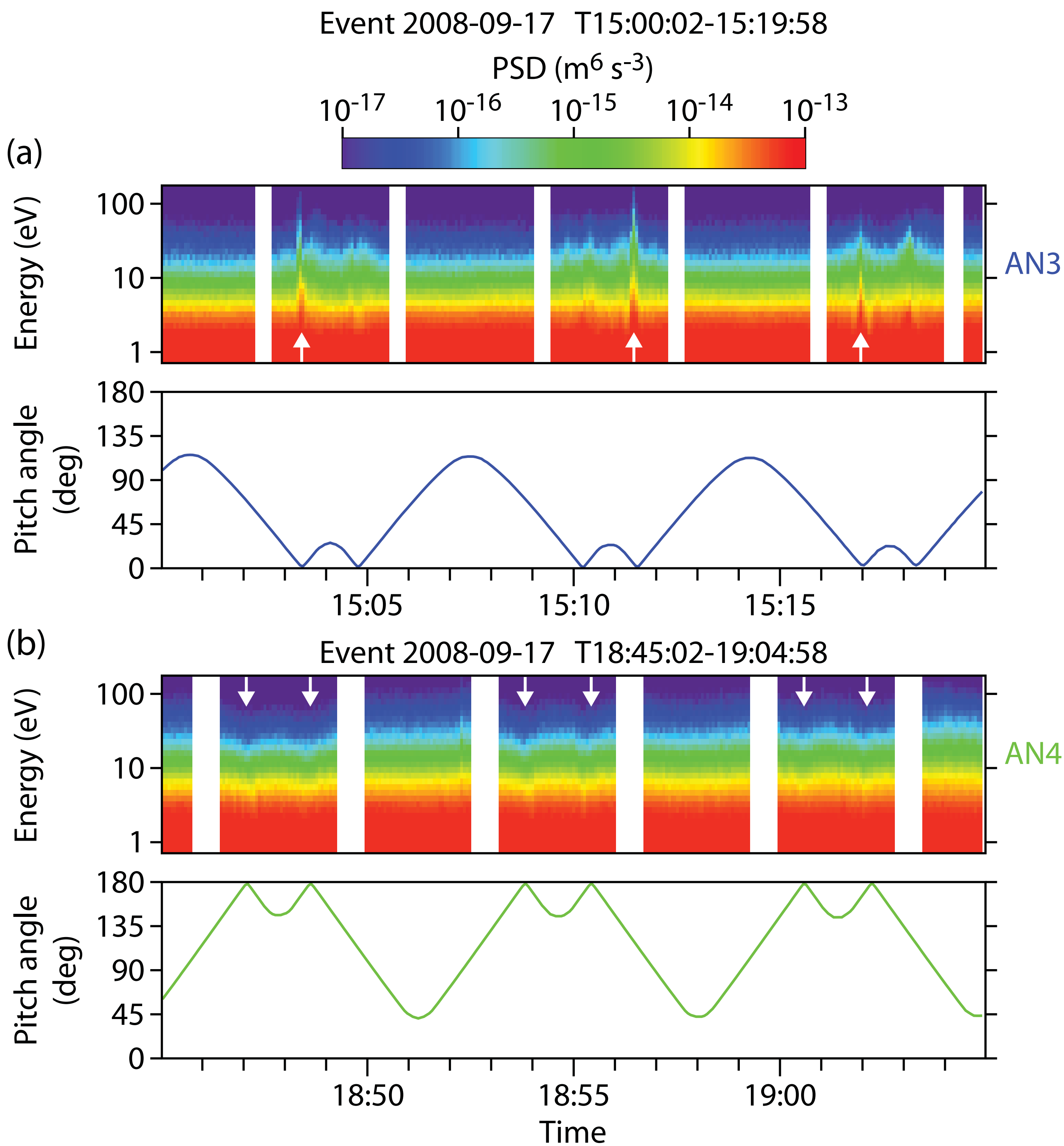
Event 2008-09-17 T15:00:02-15:19:58
PSD (m6 s-3)
10-17
10-16
10-15
10-14
10-13
(a)
Energy (eV)
100
10
1
AN3
Pitch angle (deg)
180
135
90
45
0
15:05
15:10
15:15
(b)
Event 2008-09-17 T18:45:02-19:04:58
AN4
18:50
18:55
19:00
Time

Figure 7.

A-D19-030-3

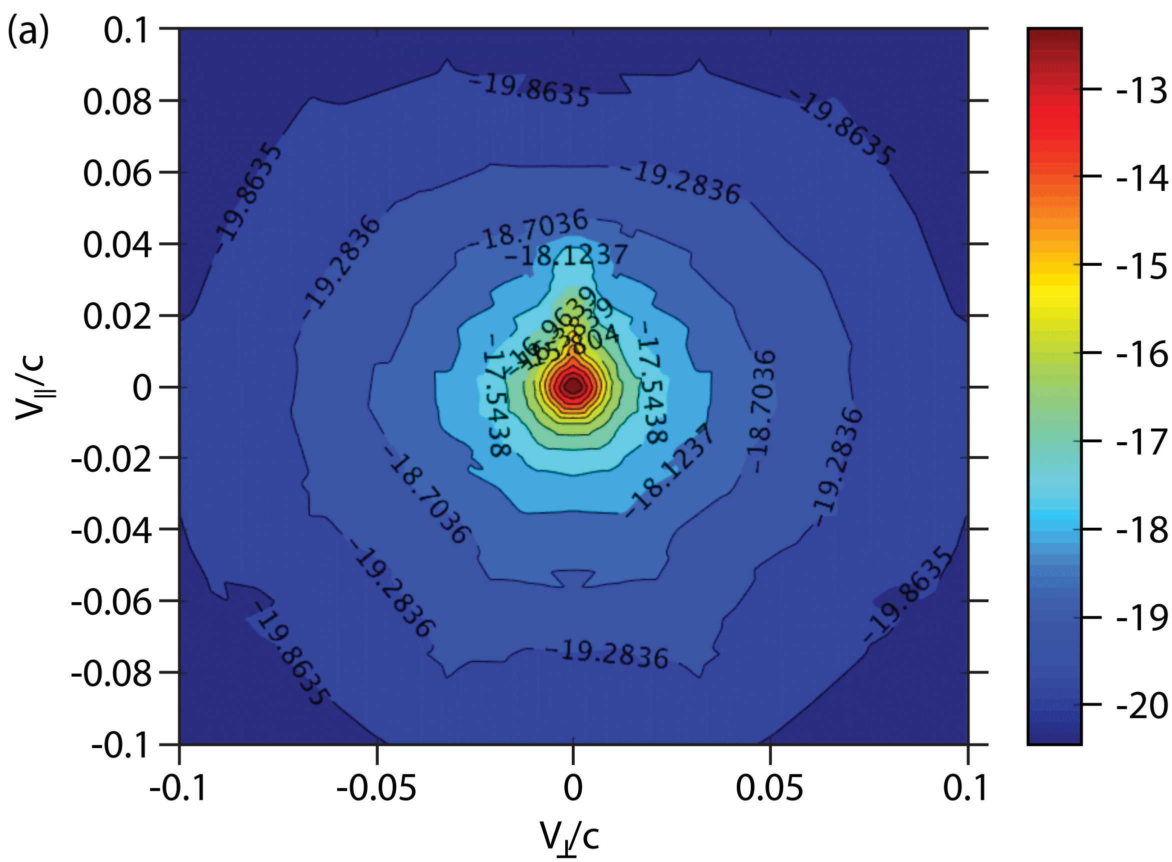

(a)
-19.8635
-19.2836
-18.7036
-18.1237
-17.5438
-18.7036
-19.2836
-18.1237
-19.2836
-19.8635
-13
-14
-15
-16
-17
-18
-19
-20
$V_{\|}/c$
$V_{\perp}/c$
0.1
0.08
0.06
0.04
0.02
0
-0.02
-0.04
-0.06
-0.08
-0.1
0.05

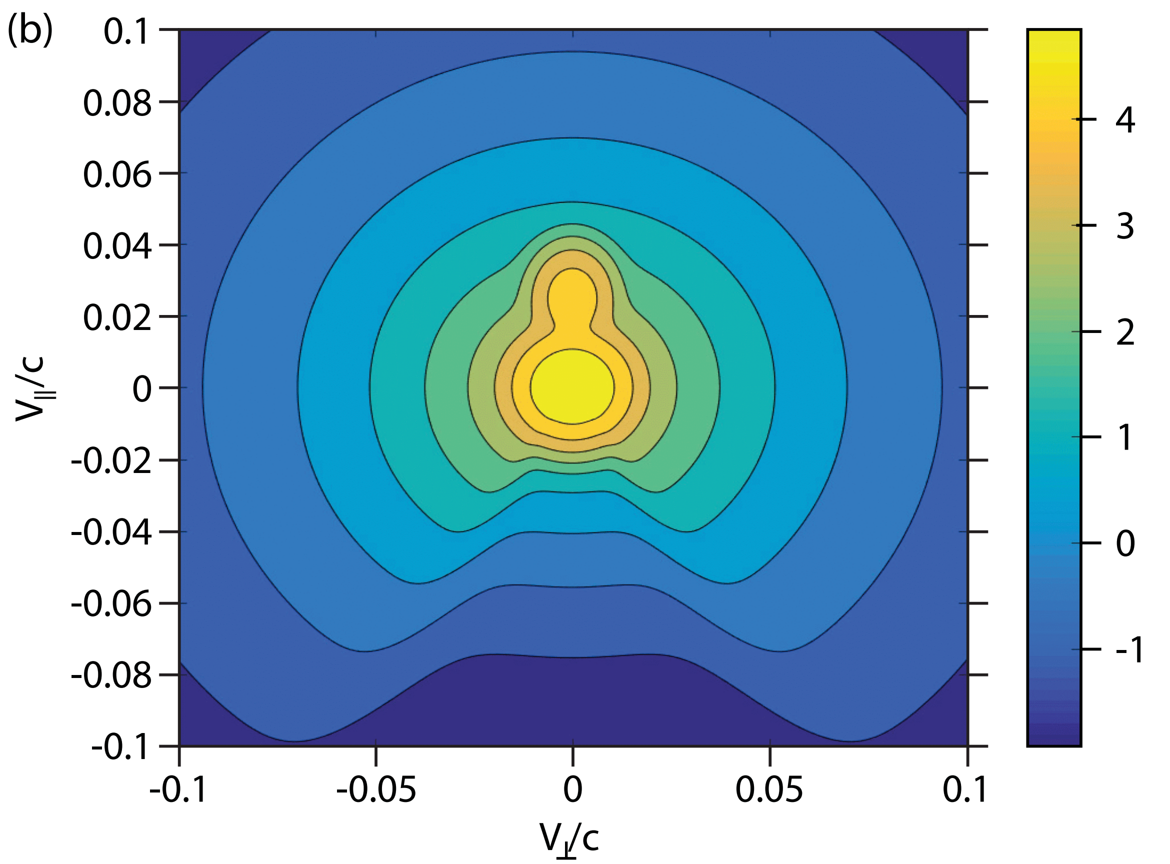

(b)
4
3
2
1
0
-1
$V_{\|}/c$
$V_{\perp}/c$
0.1
0.08
0.06
0.04
0.02
0
-0.02
-0.04
-0.06
-0.08
-0.1
-0.05
0.05

Figure 8.

A-D19-027-1

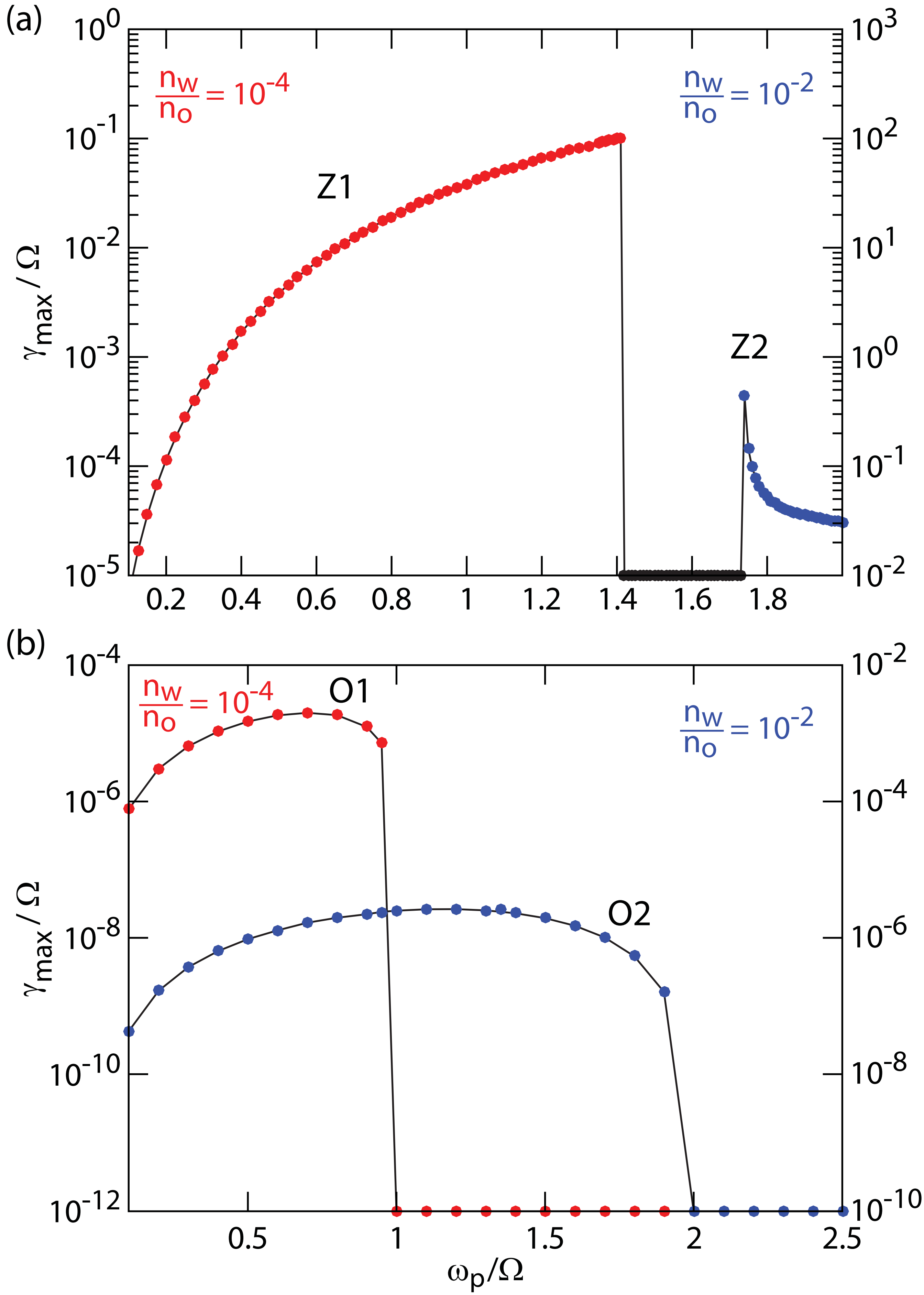

(a)
$\frac{n_w}{n_o} = 10^{-4}$
$\frac{n_w}{n_o} = 10^{-2}$
Z1
Z2
γ_{max}/Ω
10^0 10^{-1} 10^{-2} 10^{-3} 10^{-4} 10^{-5}
10^3 10^2 10^1 10^0 10^{-1} 10^{-2}
0.2 0.4 0.6 0.8 1 1.2 1.4 1.6 1.8
(b)
$\frac{n_w}{n_o} = 10^{-4}$
$\frac{n_w}{n_o} = 10^{-2}$
O1
O2
γ_{max}/Ω
10^{-4} 10^{-6} 10^{-8} 10^{-10} 10^{-12}
10^{-2} 10^{-4} 10^{-6} 10^{-8} 10^{-10}
0.5 1 1.5 2 2.5
ω_p/Ω

Figure 9.

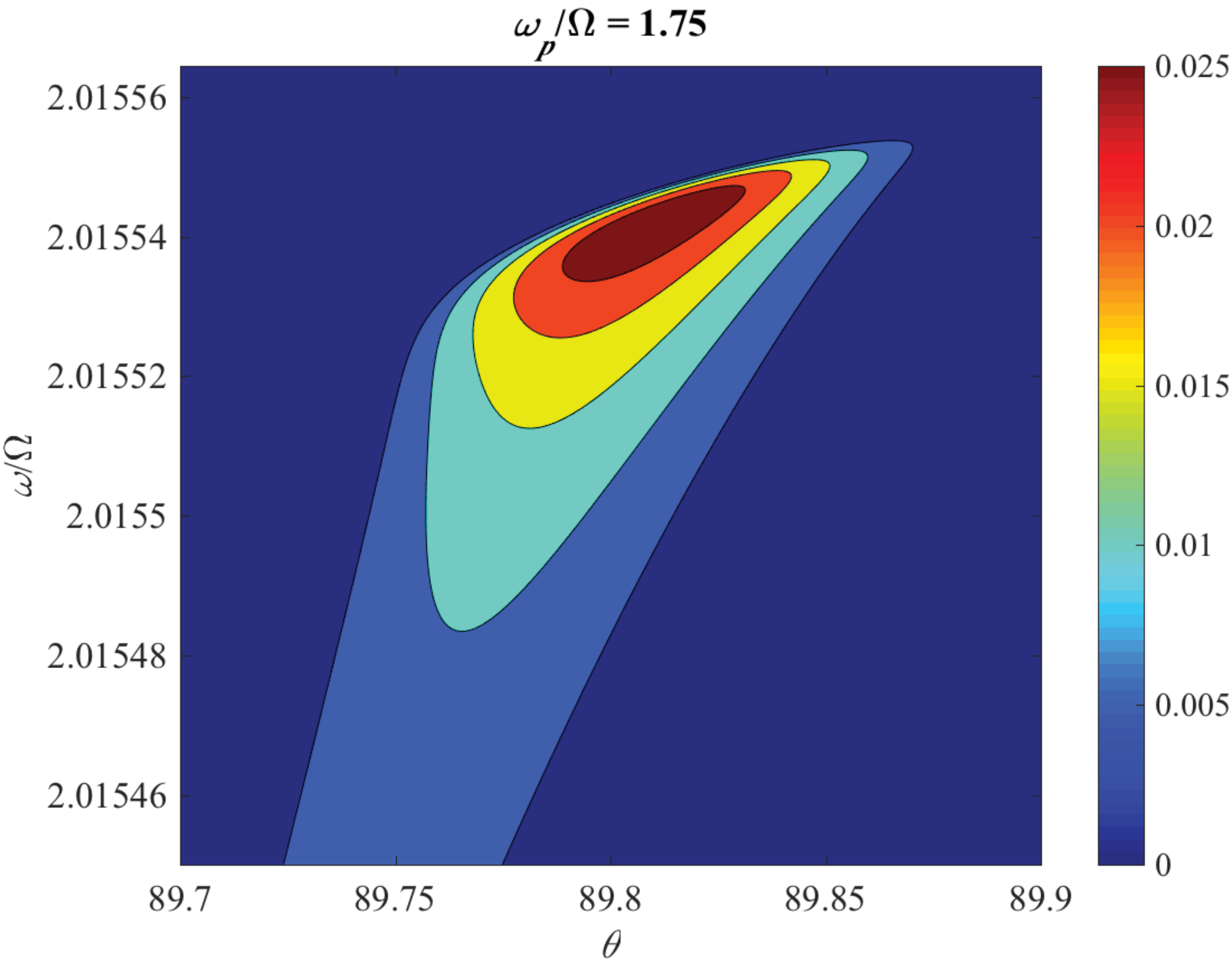

ω_p/Ω = 1.75
2.01556
2.01554
2.01552
2.0155
2.01548
2.01546
ω/Ω
89.7
89.75
89.8
89.85
89.9
θ
0.025
0.02
0.015
0.01
0.005
0
γ/Ω

Figure 10.

A-D19-028

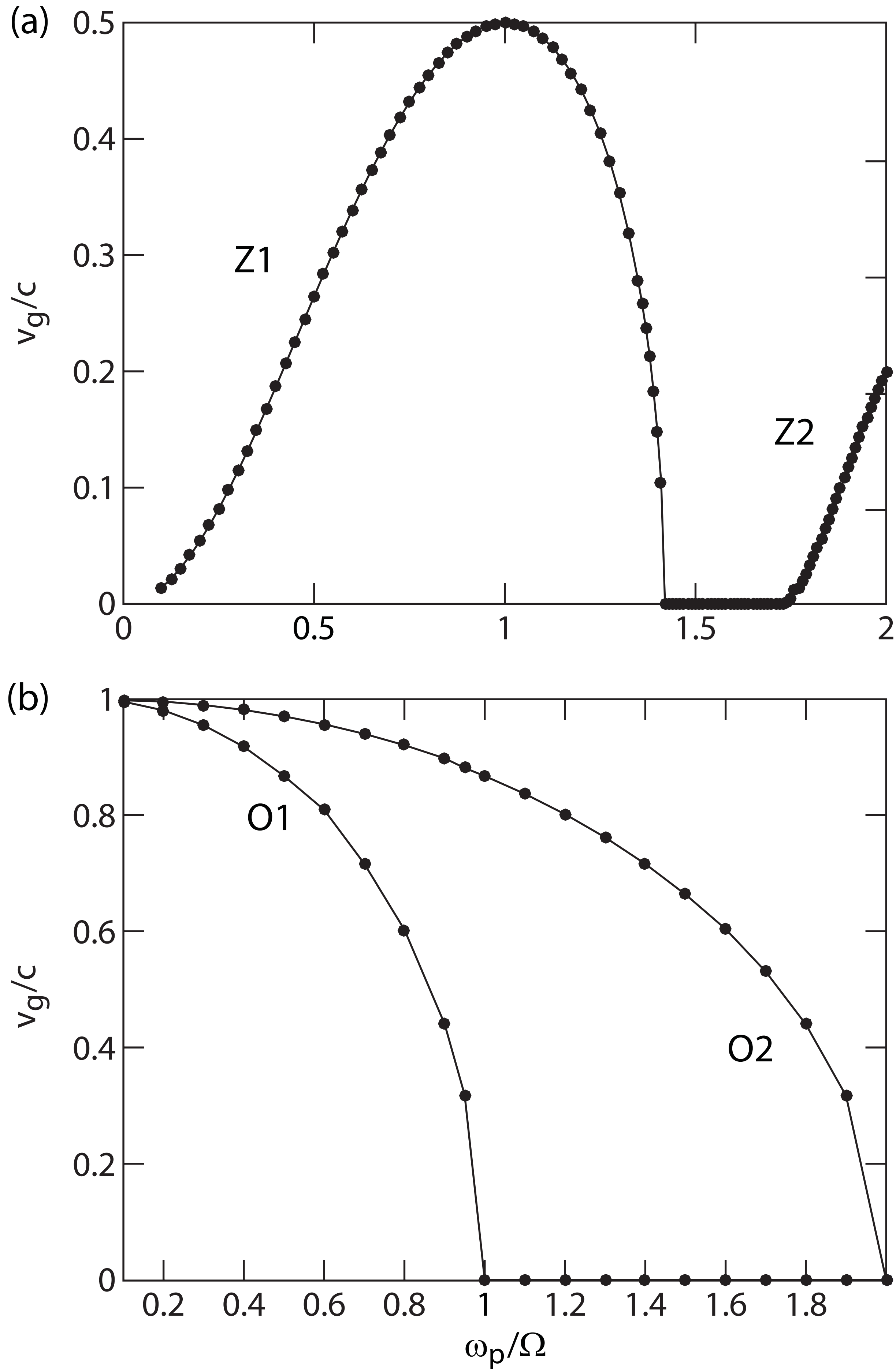

(a)
0.5
0.4
0.3
0.2
0.1
0
v_g/c
Z1
Z2
0
0.5
1
1.5
2
(b)
1
0.8
0.6
0.4
0.2
0
v_g/c
O1
O2
0.2
0.4
0.6
0.8
1
1.2
1.4
1.6
1.8
ω_p/Ω

Figure 11.

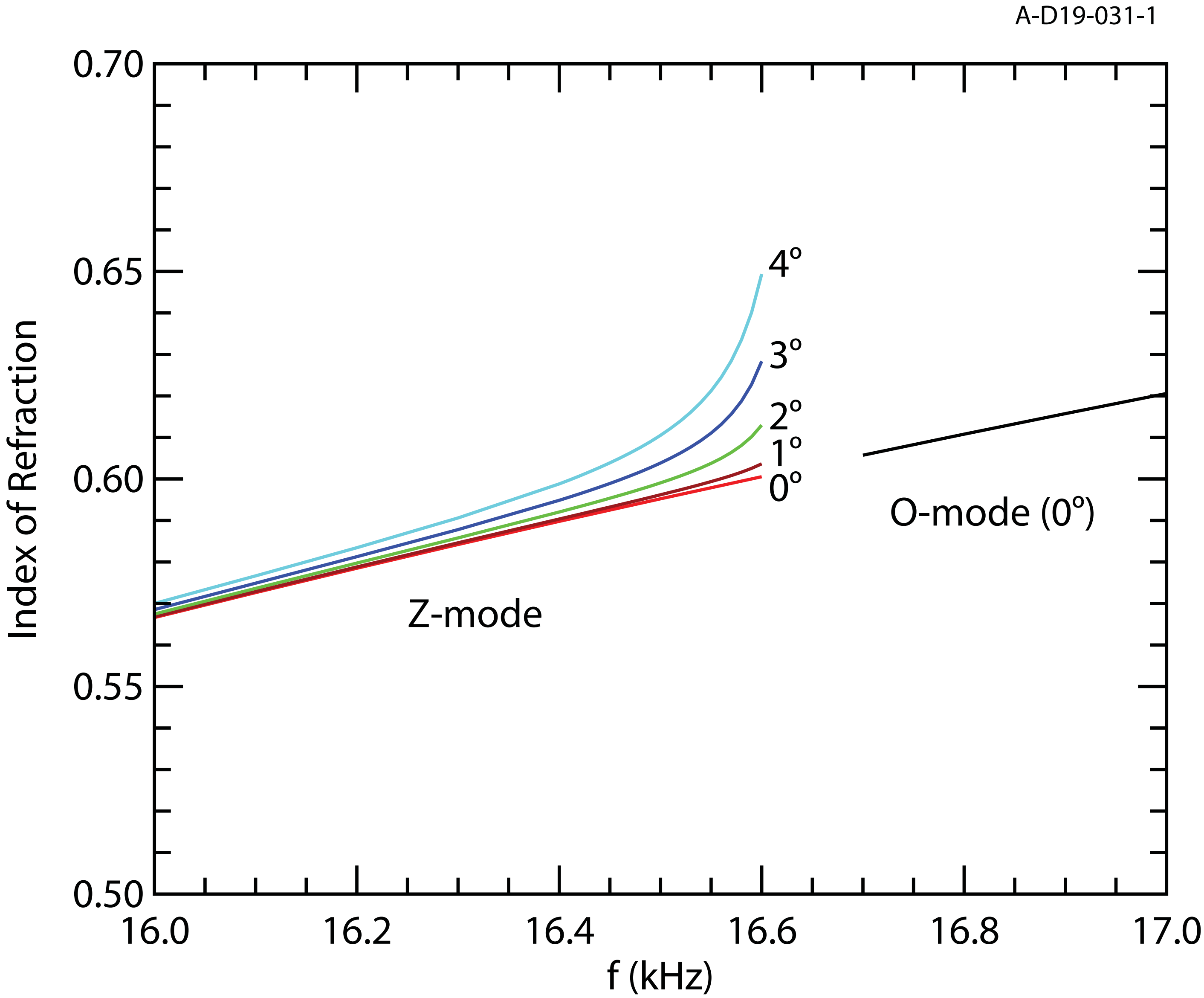
A-D19-031-1
0.70
0.65
0.60
0.55
0.50
Index of Refraction
4°
3°
2°
1°
0°
O-mode (0°)
Z-mode
16.0
16.2
16.4
16.6
16.8
17.0
f (kHz)